communications materials

A Nature Portfolio journal

Article

https://doi.org/10.1038/s43246-025-00863-7

Real-time observation of dynamic instability and adiabatic shear banding in pure titanium

Jianguo Li [1,2,3,4] ✉, Jingui Zhong[1], Longkang Li[5], Jiaming Han[1], Haosen Chen [5], Qiuming Wei [6] ✉ & Tao Suo[1,2,3,4,7] ✉

Instability of various forms is a common phenomenon in condensed matter. The adiabatic shear bands (ASBs) of visco-plastic materials attract substantial attention in both academia and industry due to their critical impact on component safety, particularly under extreme impact loading conditions. Its occurrence on an extremely small temporal and spatial scale makes prediction extremely challenging. Here, we developed an advanced in-situ testing system to capture the onset of instability and real-time evolution of deformation and temperature fields. We reported an anisotropic instability behavior in pure Ti with two distinct ASB development modes under dynamic compression in different directions. In one case, no significant temperature rise was detected until ASB propagation began; in the other, thermal softening significantly affected dynamic instability. This anisotropy is likely due to differences in dominant plasticity mechanisms. More critically, detailed experiments revealed that microstructural evolution and microscale damage are key drivers of localized plastic instability.

Ductile metals typically exhibit a peculiar, localized shear instability behavior when subjected to impact loading. This is usually signaled by a sudden stress drop on the stress-strain diagram at a certain strain, followed by a stable stress plateau[1,2]. Microscopically, the dynamic instability is accompanied by a severely concentrated thermoplastic flow in the form of bands 1.0–100 μm wide. Within these bands, the equivalent strain can reach up to 100, with the strain rate exceeding 10^5 s^{-1}. As a consequence, a large amount of heat converted from the plastic work will not have sufficient time to be dissipated out of the narrow region within such a very short period of time (a few tens of microseconds), resulting in significant local temperature rise that sometimes even exceeds the melting point of the material[3]. Due to the exceedingly short time frame and large plastic deformation in such a nearly "adiabatic" environment, the force/heat coupling easily leads to the formation of a large number of submicron/nanometer-sized equiaxed recrystallized grains[4,5]. In the recovered samples, localized shear bands with sharp boundaries at the micrometer scale can often be observed along the direction of maximum shear stress, which are usually referred to as adiabatic shear bands (ASBs)[4]. The severe shear localization naturally results in a large strain gradient in the vicinity of the ASBs, so that crack propagation along the ASBs will lead to sudden and catastrophic failure of the material or structure[6–8]. In the past century, due to its scientific and technological importance, the formation mechanism and the criterion for predicting such dynamic instability has been an important issue that has been extensively studied in the field of mechanics and materials science. However, the extremely short loading history and the very limited morphological space have posed great challenges to direct examinations. This, in turn, has seriously limited the clear understanding of the formation mechanism and the development modes of ASBs, as well as the derivation of the associated criteria for their occurrence.

The earliest and most widely accepted notion is the thermomechanical instability theory proposed by Zener and Hollomon[9]. They assume that plastic instability begins when thermal softening outplays the work-hardening of the material[9]. Experiments show that within the localized shear region, the maximum temperature rise could exceed 1000 °C along the shear axis under dynamic torsion of titanium alloys[10–12]. Following this notion, thermal perturbation or thermal softening parameters were used in the mathematical analysis and mechanistic models to stimulate the appearance of ASB during dynamic loading[3,13–15]. Although this is helpful in the qualitative understanding of the formation of dynamic shear localization in some metals, it fails in most situations in providing a reasonable and realistic

[1]School of Aeronautics, Northwestern Polytechnical University, Xi'an, China. [2]Shaanxi Key Laboratory of Impact Dynamics and Its Engineering Application, Xi'an, China. [3]Joint International Research Laboratory of Impact Dynamics and Its Engineering Application, Xi'an, China. [4]National Key Laboratory of Strength and Structural Integrity, Xi'an, China. [5]Institute of Advanced Structure Technology, Beijing Institute of Technology, Beijing, China. [6]Department of Mechanical Engineering, University of North Carolina at Charlotte, Charlotte, USA. [7]Institute of Extreme Mechanics, Northwestern Polytechnical University, Xi'an, China. ✉e-mail: lijianguo@nwpu.edu.cn; qwei@charlotte.edu; suotao@nwpu.edu.cn

prediction of the dynamic instability strain[16]. There have even been some arguments that the temperature rise prior to localization plays only a very marginal role in the formation of ASB[17]. The marginal role of temperature rises in the initiation of ASB has been verified by direct measurements of the evolution of the temperature rise during high-strain-rate deformation[18]. It was found that the accelerated and severe temperature rise was a consequence of the formation and propagation of ASB that involved an exceedingly large plastic strain over an extremely short time frame[18], as pointed out previously[17]. It should be noted that such a causal relationship between dynamic instability and temperature rise has been usually reported in metallic materials with hexagonal close-packed (HCP) crystal structure, such as titanium (Ti) and its alloys[18–21] and magnesium (Mg) alloys[17,22], where deformation twinning plays a very significant role in plastic deformation. In some aluminum alloys with face-centered cubic (FCC) structure, where plasticity is dominated by dislocation slip, in-situ temperature field measurements showed a significant temperature rise prior to instability[23,24]. During plastic deformation, some of the mechanical energy is dissipated as heat, and the remainder is stored in the material as lattice defects such as dislocations[25–27]. The amount of energy stored is directly proportional to the evolving dislocation density[26]. Deformation twins alone do not store much internal energy due to the coherent twin boundaries and should therefore release more thermal energy to increase temperature[28,29]. This is quite different from the phenomenon of no detectable temperature rise in the Ti or Mg alloys mentioned above. As such, different experimental results have been reported for different materials in terms of adiabatic temperature rise and its relationship to the formation of ASB, rendering it difficult to make comparisons to establish a causal relationship between the thermal effect and dynamic instability. More convincing and direct investigations of the evolution of the adiabatic temperature rise in specific metals are needed to gain further insights into the thermal softening effects on the plastic instability during dynamic loading.

Besides the thermo-mechanical coupling effect during dynamic deformation, micro-mechanisms are also considered to be the dominant factors preceding ASB failure, including dynamic recrystallization (DRX) softening and microdamage. This is particularly the case when the work-to-heat conversion is very limited[30–33]. As noted above, Rittel et al. demonstrated the marginal thermal effect on localized instability from energy considerations[17]. They also identified DRX grains when specimens were loaded to only half the failure strain[30]. Based on such observations, it was proposed that the early generation of DRX grains could work as weak enclaves, potentially triggering ASB formation and ultimate failure[30]. Recent advances in DRX evolution in Ti-alloys using in-situ XRD showed the onset

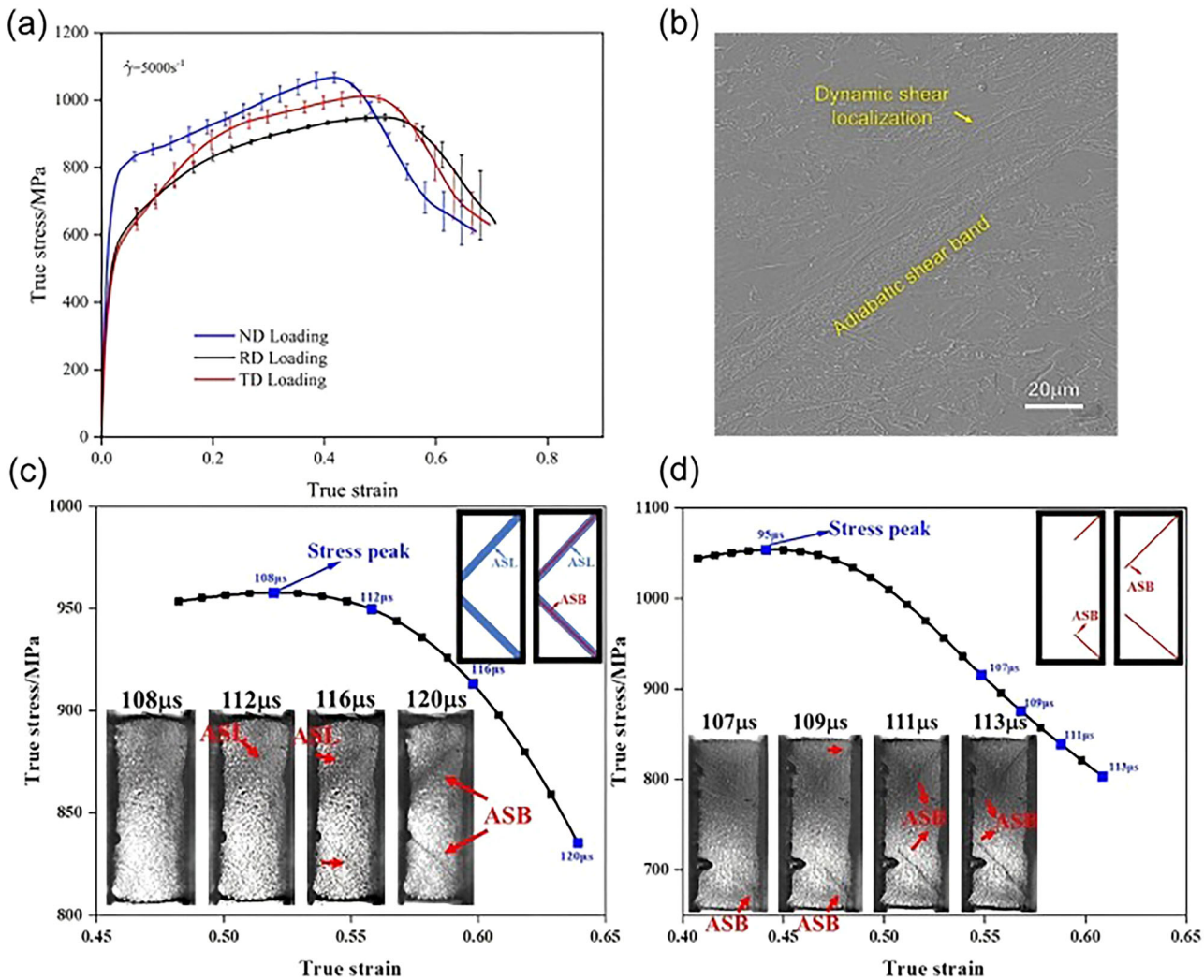

Fig. 1 | Typical mechanical responses showing the anisotropic dynamic instability behavior of the Ti specimen. a True stress-strain curves under uniaxial dynamic compression in three orthogonal directions of the specimen. The error bars indicate the deviation of the curves obtained from three repeated tests under the same conditions. **b** Microscopic morphology of ASBs in the specimen after dynamic compression along the TD; **c** and **d** Two different modes of propagation of ASBs in the specimen when loaded in the RD and ND, respectively.

of the DRX process shortly after yielding, without any association with the temperature rise[34]. Our recent work also revealed the coalescence of localized softened patches leading to the formation of ASBs in an FCC high entropy alloy[35]. However, further experimental results showed no softening effect of the DRX grains during quasi-static plasticity. It even resulted in a hardening behavior in pure Ti[36–38]. In general, it is known that grain refinement by DRX can be used to strengthen metals[39,40] if the competition between dynamic recovery and Hall-Petch strengthening is considered. Note that in most cases, under dynamic loading, the significant adiabatic temperature rise due to the conversion of plastic work to heat in the shear zone cannot be neglected. Local thermal softening must be taken into account when interpreting the occurrence of instability. But in some special cases, no heat is generated with the DRX process, similar to the quasi-static plasticity, which means no softening effect to promote the dynamic instability. This raises another very important question: if neither thermal softening nor DRX softening is involved, what other mechanisms should be responsible for the stress collapse and ultimate ASB formation? In the literature, it was also pointed out that micro-damage could serve as a local softening mechanism and lead to instability[41–46]. A similar controversy can be easily identified in the context of the causality relationship between the occurrence of microscale voids or cracks and shear instability. Traditional wisdom holds that crack propagation along the ASB is a consequence of the large shear strain within the ASB[41,44,47]. We believe the key to answering these questions is to clearly characterize the formation process of ASBs by breaking down the limitations of the temporal and spatial scales.

In this work, we established a state-of-the-art in-situ testing system to examine the evolution of deformation and the associated thermal history in real time. We then systematically analyzed the formation processes of the anisotropic dynamic instability in different loading directions for pure Ti (Grade II). Through this effort, we achieved a clear and holistic picture of the roles of heat dissipation, microstructure, or micro-damage softening in promoting dynamic shear localization and the final occurrence of ASBs. This was realized by identifying the sequence of crucial observations, including the critical instability points, adiabatic temperature rise, strain localization, initiation and propagation of ASBs, and so on. All these experiments were performed by the digital image correlation (DIC) technique and a high-speed infrared (IR) in-situ temperature field measurement system with high temporal and spatial resolutions. A plane-array IR imaging system composed of 64 × 64 InAsSb detectors was utilized to map out the temperature fields on the specimen surface. The size of each detector element is 50 × 50 μm^2. Meanwhile, on the opposite surfaces or the same surface of the cubic specimen the deformation process was recorded by a high-speed camera with a framing rate of 1×10^6 frames per second (see Supplementary Fig. 9 for details of the experimental setup). Directly measuring the field variables during dynamic uniaxial compression allowed us to investigate the entire process until the final plastic instability and failure of the specimen.

Results and discussion

Anisotropic shear instability of pure Ti under dynamic uniaxial compression

Figure1a shows the representative anisotropic dynamic instability of pure Ti in this work. More curves obtained from repeated dynamic compression tests in each direction are provided in Supplementary Fig. 2. It can be seen that when loaded in normal direction (ND), the yield strength was much higher, while maintaining a constant hardening rate until the onset of instability. In contrast, when loaded in rolling direction (RD) or transverse direction (TD), they showed similar mechanical responses in terms of lower strength and segmental hardening behavior. Additionally, their softening behavior started slightly later than that of ND. After the peak stress, there was a sudden stress drop at a critical strain, followed by a stress plateau, which usually indicates the concentrated shear flow in the ASBs. Microstructural observations after dynamic loading confirmed the appearance of ASBs, as seen in Fig.1b. More careful observations revealed a secondary localized shear region intersecting the primary ASB.

Figure1c and d display two development modes of ASBs corresponding to the anisotropic mechanical behavior. Some authors classified the nucleation of ASBs into the "strength-like" and "toughness-like" modes, depending on specimen geometries and loading conditions in various metals[24,48]. Our work provides the first evidence for different development modes of ASB in the same material and under the same loading condition. As can be seen from the high-speed visual recording images in Fig.1c, two adiabatic shear localization (ASL) zones appeared first, and then the ASBs ran through the shear zones instantaneously. In contrast, in Fig.1d, ASBs nucleated at the specimen's corner and extended like a crack to the opposite edge. To more clearly describe the different development modes of ASBs, we added two insets of schematic sketches in the upper right corner of Fig. 1c and d, respectively. Such anisotropic instability behavior or different formation processes were indeed associated with the different plasticity modes and dominant instability mechanisms when loaded in different directions. Supplementary Fig. 4 showed the microstructural features and corresponding pole figures, revealing an obvious rolling basal texture. As illustrated by the crystal lattice orientation of each grain in Supplementary Fig. 4a, the c-axes of most grains were closely parallel to the ND of the rolling plate. Therefore, it is not difficult to understand the dynamic anisotropy of pure Ti. Correspondingly, we also calculated the Schmid factors for the predominant slip system in HCP metals (see Supplementary Fig. 5). When the specimens were loaded in the RD and TD, they had similar potential slip systems. This was why they showed similar mechanical responses and the same ASB formation mode. However, when loaded in the ND, only the pyramidal <c+a> slip systems were the potential ones with larger Schmid factors. In Supplementary Fig. 6, we have shown the evolution of microstructural features with increasing strain when loaded in different directions, particularly the labeling of deformation twin types. Apparently, when loaded in the RD/TD directions, the specimens were plastically deformed via a combination of dislocations in large grains and deformation twins (DTs) in some smaller grains. At lower strains, more extension twins (ETs) were activated, but as the strain increased, fewer ETs remained, and the total number of DTs decreased dramatically. In contrast, when loaded in ND, the plasticity of almost all grains was apparently mediated by deformation twins and dominated by contraction twins (CTs). We also analyzed the evolution of dislocation density using electron backscatter diffraction (EBSD) mapping and Kernel average misorientation (KAM) analysis in Supplementary Fig. 7. Here we were more concerned with the change in dislocation density due to the hindering effect of deformation twins on dislocation slip[49,50]. Obviously, when loaded in RD/TD, dislocation density was much higher in grains where deformation twins were activated. In some grains without twins, dislocations were trapped near the grain boundaries. In comparison, since the deformation twins were activated in almost every grain, the dislocation density of local regions at $\varepsilon = 0.2$ has already reached a very high value of $2 \times 10^{15}/m^2$. With increasing strain, the grains continued to store up more dislocations. In the following discussion, such dislocation distribution results can also help us understand the different temperature field measurement results. As described above, different plasticity mechanisms will lead to different microstructural evolution and heat dissipation during dynamic deformation[25,27–29]. This allows us to further determine the primary softening mechanisms conducive to dynamic instability.

In this paper, we will elaborate on the instability mechanisms of ASBs in different modes based on a more in-depth analysis of the experimental results. Here, in the main text, we focus on the results of RD and ND for comparison. Other similar results can be found in the Supplementary Materials. (See Supplementary Fig. 8 for the microscale morphology of ASBs after loading in RD and ND, and Supplementary Fig. 10 for the formation process of ASBs in TD-loaded specimens). We also confirmed the different development modes of ASBs when the specimens were loaded in different directions using high-speed in-situ visual recording and temperature field measurements on the same surface of the cubic specimen. In Supplementary Fig. 11a, the high-speed recording images as loaded in the RD showed the variation in shading degree along the shear direction. This indicates the formation of localized shear zones at first, followed by an instantaneous

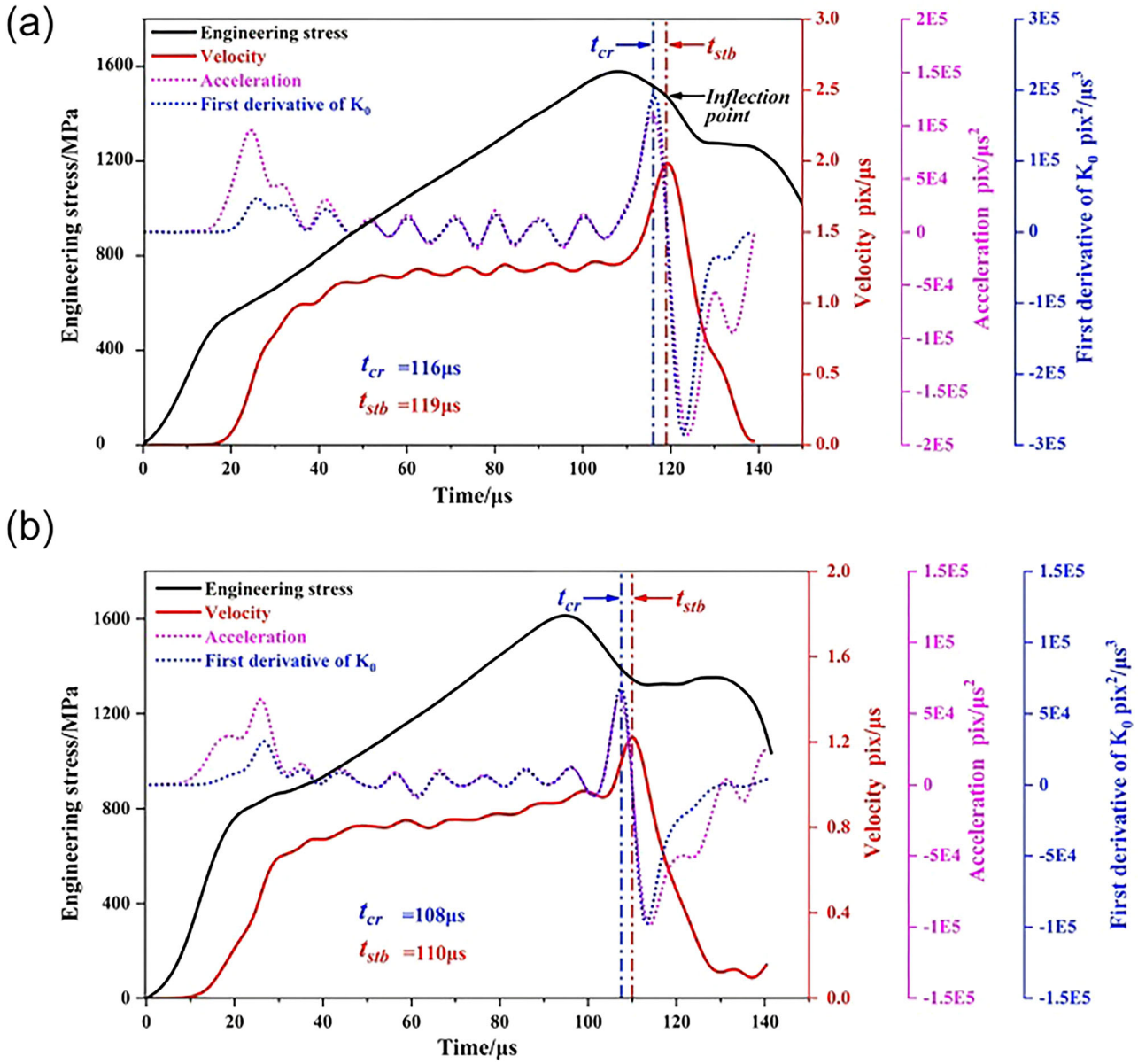

Fig. 2 | Determination of the critical instability time by tracking the evolution of the velocity of characteristic points on the surface of the cuboidal specimens during uniaxial dynamic compression in different loading directions. a Rolling direction and **b** Normal direction.

expansion of the ASBs, leading to complete instability. Similarly, when loaded in the TD, the strain field results in Supplementary Fig. 11b also showed the appearance of shear localization, and then the ASBs immediately extended through the shear zones to result in instability at a critical time. Differently, when loaded in the ND, the ASBs started to propagate from the left edge of the specimen at the critical instability time and gradually extended to the opposite edge along the shear direction (see Supplementary Fig. 11c).

Accurate determination of the critical instability points

Naturally, the first step in studying the evolution of ASBs is to assess the critical moment when the instability occurs. Conventional wisdom holds that the onset of stress collapse in the dynamic stress-strain curve signals the onset of dynamic instability. To substantiate this notion, high-speed photography has been used to pinpoint the critical time. However, the extremely short duration and the very small length scale of ASBs involved make it difficult to guarantee the precision of this approach. In this work, we used a physical parameter of the surface particle velocity according to a kinetic energy-based localization theory proposed by Cherukuri and Shawki[51,52]. In the first part of the Supplementary Information, we provided a detailed description of the derivation of this theory. In this theory, the onset of shear instability was related to the rate of kinetic energy. As shown in Supplementary Fig. 12, we selected the specific specks outside the shear regions as the characteristic points to follow the evolution of their velocities. The first derivative of the kinetic energy per unit mass was expressed as the product of velocity (red curve) and acceleration (pink dotted curve in Fig. 2). Namely, its change rate with time was used, as plotted as the blue dotted curve in Fig. 2. The peak value of the change rate then indicated the critical instability time (t_{cr}). After this point, plastic deformation was completely concentrated in the ASBs, and the acceleration of the characteristic point started to decrease until it reached zero. At that point (t_{stb}), deformation transitioned into a steady flow stage within the ASBs. It is intriguing to note an inflection point on the mechanical curve (or the stress-time curve in black) of Fig. 2a. Due to the complete loss of stability, the flow stress started to drop again. Then, since the end of the transmitter bar obstructed the motion of the specimen (see the high-speed camera snapshot in Fig.1c), the acceleration became negative. As such, the dynamic load was supported by the whole specimen, and the mechanical curve entered a constant flow stage (see

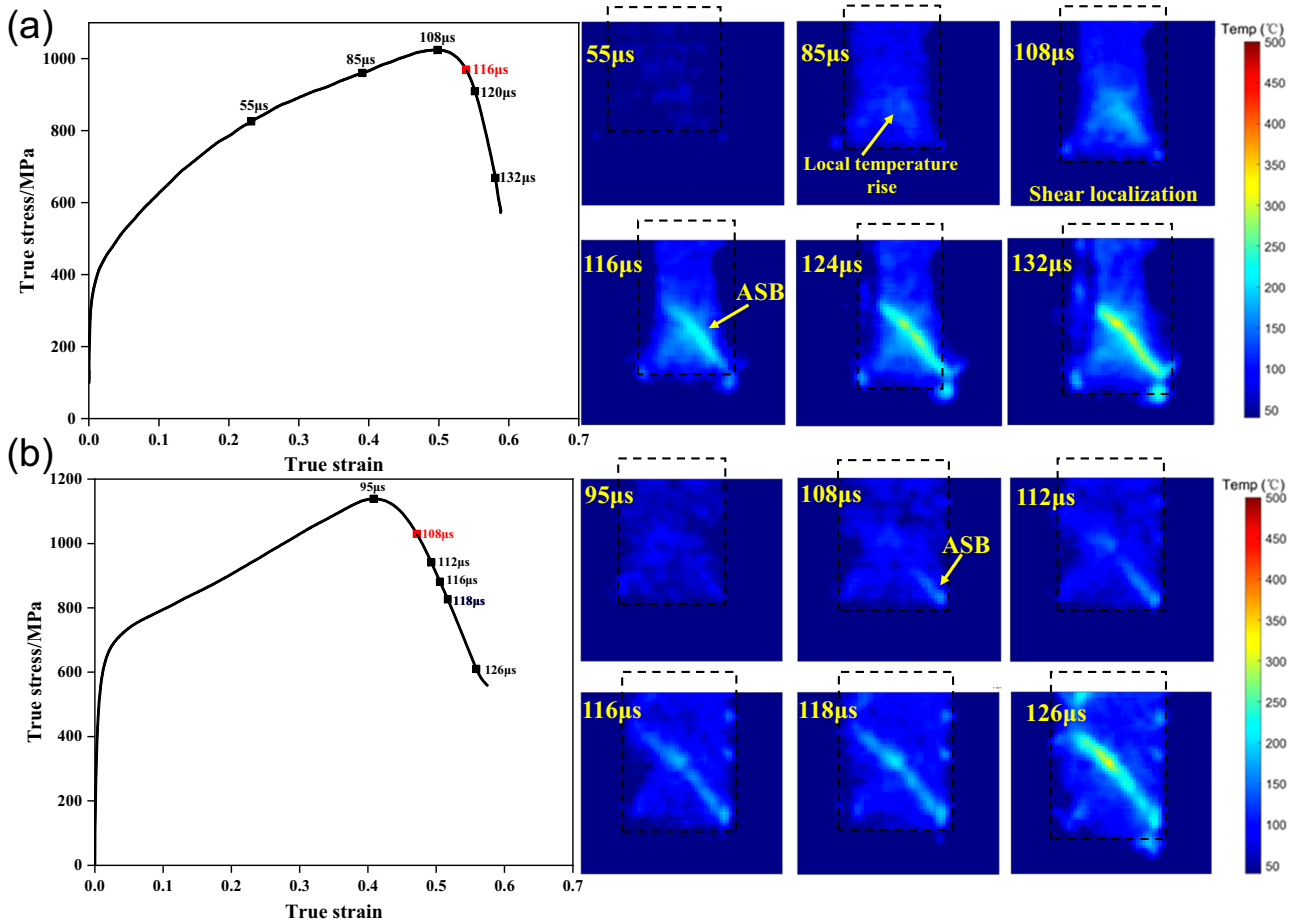

Fig. 3 | The evolution of in-situ temperature fields on the specimen surfaces during dynamic compression in different loading directions. a Rolling direction and **b** Normal direction.

Supplementary Fig. 12b for the measurement results of kinetic parameters on the TD-loaded specimen). When loaded in the ND, the specimen experienced a similar deformation and instability process. But its instability came relatively late, and the transition to a constant stress plateau occurred faster (Fig. 2b). This is related to the different development mode of ASBs in this loading direction. In the following sections, we will further discuss the dominant instability mechanisms behind the different formation modes of ASBs.

The role of thermal softening in dynamic instability

This is the first controversial issue addressed in this paper. By combining critical instability measurements with real-time temperature field data, we explicitly clarified the causality between adiabatic temperature rise and shear instability. Limited by the measurable area of the high-speed IR system (3.2 mm × 3.2 mm), we captured the temperature field evolution of one wing of the two conjugated ASBs. In Fig. 3, the black dashed rectangular shapes mark the temporal shape changes of half of the specimen, while the color changes in this area showed the temperature field evolution on the specimen surface. Notice in particular that the temperature rises within the shear region. Except for the localized shear zones, the temperature rise was less than 100 °C, which should only have a marginal effect on the specimen's mechanical response. However, with the development of shear localization/ASBs, a significant temperature rise was observed. Moreover, different development modes of ASBs led to different temperature rise patterns within the shear zones. When loaded in the RD (Fig. 3a), the temperature at a local site along the shear direction had risen to more than 200 °C (at 85μs). As deformation continued to the peak stress (108μs), the local temperature rise became more substantial. Finally, dynamic instability occurred at a critical time, which was captured as a concentrated hot region through the specimen. Subsequently, due to concentrated shear flow, the highest temperature in the ASBs exceeded 400 °C. In this case, thermal softening in the local region should be a primary contributor to instability. Furthermore, the microstructure evolution (such as DRX) in this shear region, caused by coupling effects of large strain and high temperature, should also be carefully addressed. This will be discussed in the next section. Similar temperature fields measured on the TD-loaded specimen can be found in Supplementary Fig. 13. On the contrary, when loaded in the ND, no significant temperature rise was detected before the critical instability. A significant temperature rise appeared only with the propagation of ASBs at the critical instability time of 108μs. This means that the temperature rise is a result of shear instability. In this specimen with profuse twinning, the higher density of stored dislocations due to the twinning hindrance effect[49,50] resulted in more strain energy storage (see Supplementary Fig. 7) and hence lower plastic work conversion to heat. Furthermore, from the temperature field evolution when loaded in different directions, we could clearly distinguish the different development modes of ASBs. When loaded in the RD/TD, the ASB appeared in a wider localized shear zone and immediately extended through the specimen at the onset of instability. However, when loaded in the ND, the ASBs first appeared at the the specimen's corners and then gradually extended to the opposite side along the shear direction. We could even see a clear deflection of the ASB after a certain propagation distance (see the temperature field at 112 μs). It is important to note that the temperature fields (Fig. 3a and b) and high-speed camera images (Fig. 1c and d) were taken separately on the opposite surfaces of the cubic specimen but correspondingly showed the identical development patterns of ASBs. This further demonstrated the plausibility of our understanding of the different development modes of

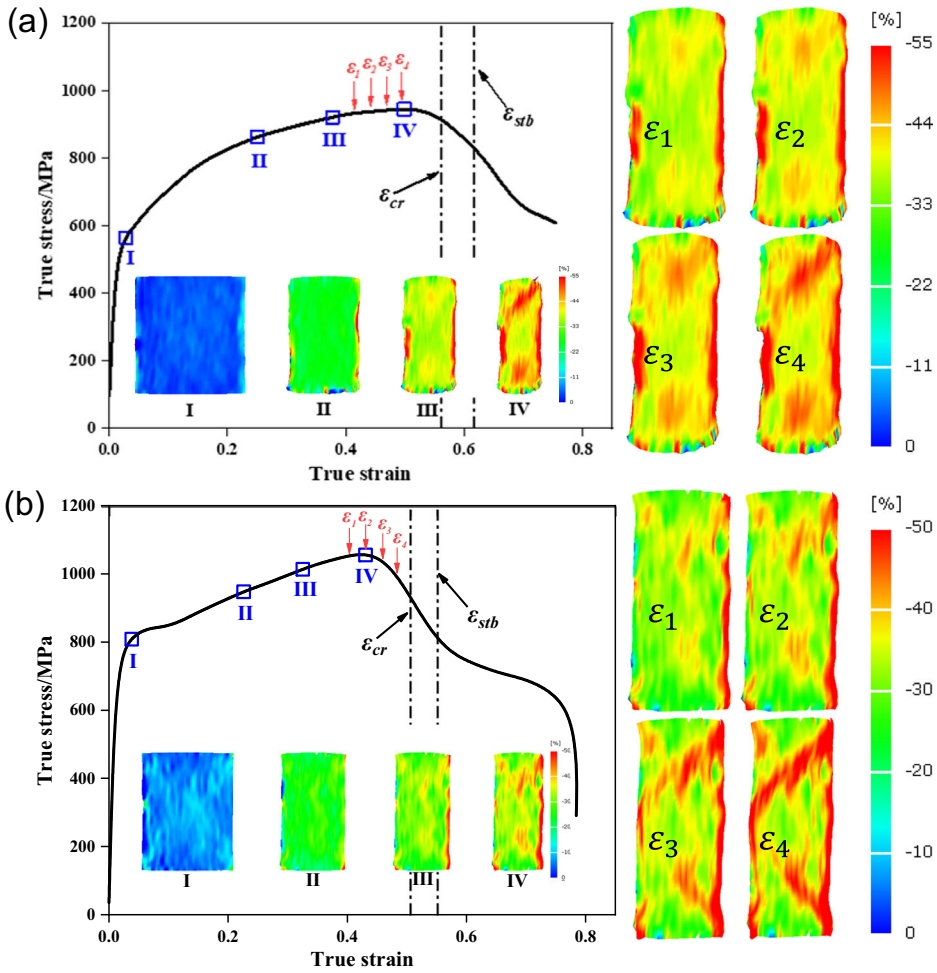

Fig. 4 | The evolution of in-situ strain fields on the specimen surfaces during dynamic compression in different loading directions. a Rolling direction and **b** Normal direction.

ASBs. In addition, we provided in-situ temperature field measurement results obtained on a single surface of the cubic specimen in Supplementary Fig. 14, corresponding to the high-speed visual recording and strain field test surface. The same evolution process of adiabatic temperature rise within the shear zones and ASBs confirmed again the differences in the occurrence of dynamic instability as loaded in different directions. By combining more detailed microstructure evolution below, we will provide more convincing analyses of the dynamic instability mechanisms.

As discussed above, due to the localized shear deformation under dynamic compression, the conversion of plastic work into heat results in a significant adiabatic temperature rise. Meanwhile, it will be seen in the next section that dynamic localization is also the major cause of microstructure evolution. Therefore, it is very important to acquire the strain fields to analyze the whole deformation process. In Fig. 4, the DIC results showed the strain evolution of the specimens when loaded in the RD and ND, respectively (see Supplementary Fig. 15 for the strain evolution when loaded in the TD). It is evident that when loaded in the RD/TD, the localized shear zone has passed through the specimen along the shear direction before the peak stress (see strain field pattern at ε_4 in Fig. 4a). Severe plastic concentration can lead to more conversion of plastic work to heat, and therefore we have already observed significant adiabatic temperature rise in a wide shear zone at the peak stress. Then, considering the coupling effects of thermal softening and further microstructural evolution in this local region, it is easy to understand the subsequent instantaneous dynamic instability. However, when loaded in the ND, only sporadic scattered shear regions were observed along the shear direction prior to the peak stress (see strain field pattern at ε_2 in Fig. 4b). As the strain increased, the shear localization began to extend through the specimen. Note that before the critical instability strain (ε_{cr}), no temperature rise was detected at this moment. This is understandable as more strain energy was stored during plastic deformation. Supplementary Fig. 7 showed profuse DTs in the ND-loaded specimen. Usually, DTs are thought of as an athermal process, and because of the coherent twin boundaries, DTs alone do not store strain energy. Some authors reported enhanced heat production by twinning[28,29]. However, as reported by Lu et al.[49], the plastic straining of even nano-twinned copper is accompanied by the multiplication of very high density of dislocations. A similar phenomenon has been observed in twin-induced plasticity (TWIP) steels[50]. Our observations are in line with such literature results in that comparing the twinning effects on the dislocation density evolution in Supplementary Fig. 7b–f, a higher fraction of deformation twins resulted in a much higher dislocation density. This means that although the DTs themselves did not store plastic energy, they often significantly facilitate the storage of dislocations and thus increased the plastic energy storage to reduce the work-to-heat conversion rate. Such a notion helps to understand no significant temperature rise during the stable plasticity in the ND-loaded specimen. Nevertheless, another very important phenomenon based on the strain field evolution should be stressed here. That is, although there was no thermal softening, the connectivity of discretely distributed local deformation sites (see the strain fields at ε_3 and ε_4 in Fig. 4b) started to cause stress reduction and ultimate instability along the shear direction. This should be associated with the microstructural evolution in these shear regions. Next, we will delve into the microstructural evolution to further understand the instability mechanisms.

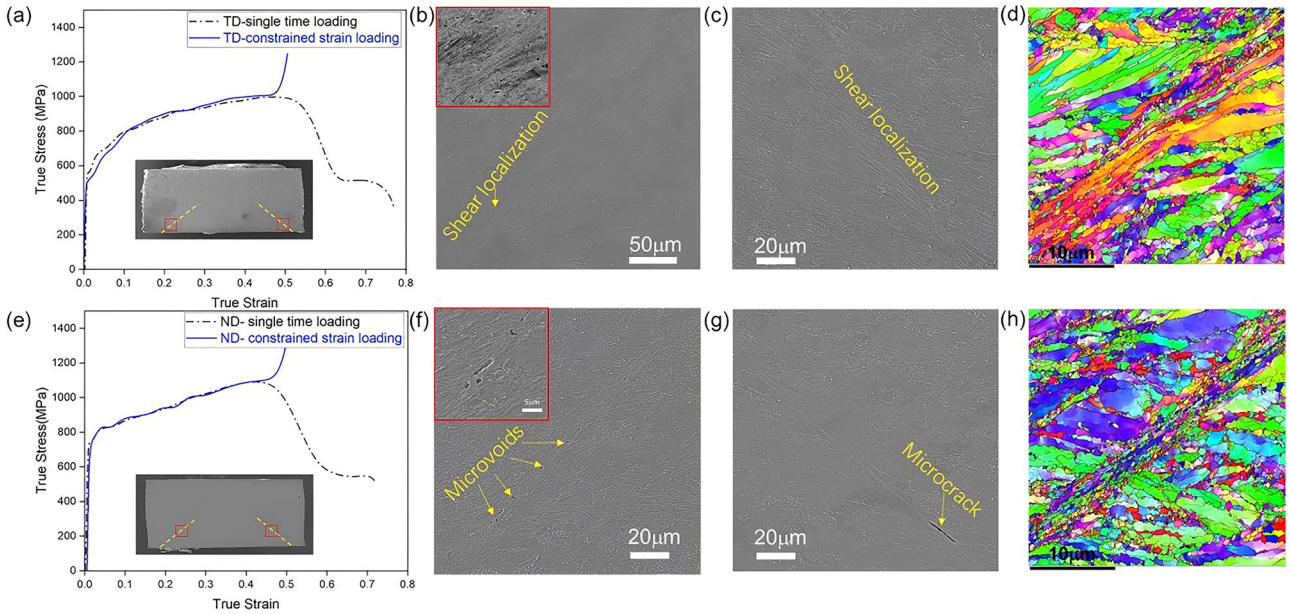

Fig. 5 | Typical mechanical responses when the specimens were loaded to a given strain near the peak stress in different directions, and the corresponding microscale morphology of shear localizations and microstructural observations within the localized shear regions are also shown. a and **e** comparisons of mechanical responses between the constrained strain loading (blue solid curve) and single loading (black dotted curve) in different directions, while the further observation locations on the specimens are marked by red boxes; (**b**, **c**) and **f**, **g** SEM images showing the morphological features after dynamic compression to a given strain; **d** and **h** EBSD mapping results showing the variations within the localized shear regions.

Roles of microstructure/micro-damage softening in dynamic instability

Two more controversial issues associated with the occurrence of ASBs remain to be clarified. They are related to the microstructure evolution during plasticity. The first concerns the appearance of DRX grains. In this context, we loaded the compression specimens in different directions to a prescribed strain (close to the peak stress, blue curve in Fig. 5a and e). From the strain fields of the localized deformation zones, we could find conjugated localized shear bands near the edge of the specimens. These bands only expanded through half of the specimen along the shear directions, as indicated by the yellow dashed lines in the SEM images of Fig. 5a and e. For the TD-loaded specimen, the enlarged SEM images in Fig. 5b and c clearly showed the canonical pattern of shear flows in the sense of Wright[53]. The band contrast (BC) map in the left corner presented the localized shear at much higher magnification. More specifically, the EBSD mapping of Fig. 5d showed numerous dynamic recoveries with a few DRX grains in the shear zone. Of particular interest is the predominance of low-angle grain boundaries (red curves in the EBSD map of Fig. 5d) within this shear zone due to the dislocation-dominated plasticity. During subsequent plastic deformation, the coupled adiabatic temperature rise effect then gradually caused more severe DRX, which finally triggered the onset of dynamic instability. The RD-loaded specimen exhibited similar microstructure evolution and mechanical behavior due to similar plasticity mechanisms that were dislocation-dominated and twin-assisted.

On the contrary, when loaded in the ND, the dominant plasticity mechanism changes to deformation twinning. It has been widely documented that twin interactions or dislocation fragmentation between twin boundaries strongly favors the occurrence of DRX, and thus the term "twinning-induced DRX" (TDRX)[36,54–56]. As such, we were able to see localized shear bands with distinct boundaries in samples at the prescribed strain near the peak stress, consistent with previous observations[24]. We believed that this should be a result of DRX in the large deformed regions along the shear direction. In Fig. 5h, the EBSD mapping clearly showed a remarkable number of DRX grains with high-angle grain boundaries. It is important to note here that although severe DRX occurred in the localized regions, no softening occurred until the end of the strain constraint. TEM observations of the DRX grains within the shear region, as shown in Supplementary Fig. 16, revealed that the submicron lamellar grains were filled with high density of dislocations. This is consistent with some published results where grain refinement via continuous DRX during severe plastic deformation has been used to strengthen metals[39,40]. As such, this leads to an important question as to why a significant stress drop followed by complete instability occurred without any detectable temperature rise or microstructural softening. Full-field strain measurements with detailed microscale observations revealed continuous local shear zones throughout the specimen. Additionally, massive micro-voids and microcrack appeared in these local bands, as shown in Fig. 5f and g. In the upper left magnified micrograph of Fig. 5f, we could even see microcracks presumably formed through the coalescence of voids. It is reasonable to believe that the accumulation of concentrated shear strain tends to cause more nucleation of microscale voids or cracks due to the relatively low plastic deformation capacity of the very small DRXed grains in pure Ti[57–59]. Meanwhile, these experimental observations provide convincing evidence to clarify the third controversial issue about the casual relationship between microdamage and dynamic instability. It is certain that microscopic damage is indeed one of the critical factors inducing adiabatic shear instability.

Conclusions

To summarize, in this work, we have reported two different development modes of ASBs in pure Ti, indicating an anisotropic dynamic instability when dynamically compressed in different directions due to the pre-existing basal texture. Using in-situ deformation field measurements of the velocity of characteristic points on the specimen surface, we accurately determined the critical time for instability. We found that complete instability occurred in a very short time after the peak stress. Subsequently, simultaneous measurements of high-speed infrared temperature fields and strain fields, combined with detailed microstructural observations, clearly revealed the controlling instability mechanisms corresponding to the different ASB modes. In particular, several long-standing controversies in the research area have been clarified. These include the causal relationship between adiabatic temperature rise, DRX/microdamage, and dynamic instability, which depends primarily on the dominant plasticity mechanisms of the

materials. In the dislocation-dominated specimen, thermal softening coupled with microstructural evolution triggered the instability to form ASBs. In the twinning-dominated case, DRX-induced microdamage in the local shear zones should be responsible for the ultimate instability and the appearance of ASBs, with the adiabatic temperature rise being a result of dynamic instability. Such a comprehensive understanding of the different instability mechanisms in pure Ti can provide a solid basis for the further development of mechanistic and mathematical theories of ASBs, especially with crystal plasticity modeling.

Methods

Material and mechanical tests

The rolled commercial pure titanium plate of 99.5% purity (TA2) in the recrystallized state was used to cut the cubic specimens in this work. The three-dimensional size of the dynamic compression specimen is 3 × 3 × 3 mm^3. Please refer to Supplementary Fig. 3 for the initial dimensions of the cubic specimens before dynamic compression, meanwhile, the representative morphological features after dynamic instability are also given. In order to consider the texture effect on the mechanical behavior, we conducted high-strain-rate uniaxial compression tests along three orthogonal directions of the cubic specimen. The standard Split Hopkinson Pressure Bar (SPHB) system was used to obtain the dynamic mechanical response at ambient temperature. The striker bar, incident bar and transmit bar were all made of maraging steel and had a diameter of 12.7 mm. After the conventional dynamic compression test, the engineering stress (σ_e), engineering strain (ε_e) and strain rate ($\dot{\varepsilon}$) of the tested specimen can be obtained by processing the recorded stress wave signals based on the one-dimensional stress wave theory. In this work, the compressive loading rate was set to approximately 5 × 10^3 s^{-1}. Routinely, at least three repeated tests were performed under each loading direction to ensure the reproducibility of the results.

High-speed in-situ strain and temperature field measurements

During the dynamic compression experiments, a high-speed photography system, consisting of an ultra-high-speed camera (Kirana), a telecentric lens, and flash lamps, was used to record the deformation process. The camera framing rate was set to 1 × 10^6 frames per second, and it could record 180 consecutive photos when triggered. The total recording duration was therefore 180 μs, ensuring that the entire deformation process was captured. For more quantitative information, we sprayed randomly distributed speckles on one of the specimen surfaces. The digital image correlation (DIC) technique was used to track the velocity evolution of the selected characteristic points and to calculate the strain field of the specimen surface at different loading times. Meanwhile, a high-speed infrared (IR) temperature field measurement system, which was composed of 64 × 64 InAsSb detectors arranged in an array with very small spacing between adjacent detectors (~1 μm), was used to record the evolution of the adiabatic temperature rise during impacts. The size of each detector was 50 μm × 50 μm, resulting in a detectable area of 3.2 × 3.2 mm^2. The response time of the thermal detectors was 1 μs. They received the radiation signal from the object, converted it into a voltage, and then stored it as the grayscale image. Prior to testing, the detectors were calibrated to establish the correlation between temperature and grayscale value. The temperature-gray-value correlation then became the basis for retrieving the true temperature. The recorded grayscale images were converted into temperature fields at different loading times. The detectable temperature ranged from 30 °C to 800 °C. All of the above high-speed test instruments together form the in-situ strain and temperature field measurement system. Supplementary Fig. 9 illustrates the schematic and real experimental setups, showing the details of each unit. Due to the obstruction of the temperature measurement system, we had to place the high-speed camera on the opposite side. This meant that we could only directly measure the deformation process and the temperature evolution separately on the two opposite surfaces of the cubic specimen. To achieve simultaneous recording of the high-speed visual images and the temperature field evolution on the same surface, we placed a fully reflective mirror underneath the optical path of the temperature measurement system. The mirror was tilted at an angle of approximately 12° from the vertical direction, allowing the image of the back surface of the cubic specimen to be reflected to the high-speed camera. This setup enabled simultaneous measurements of the deformation and temperature evolution on a single surface. To reduce the potential inaccuracies of temperature measurement, we only sprayed half of the sample surface with randomly distributed speckles to simultaneously obtain the strain fields. The results from the opposite surfaces and the same surface showed excellent consistency. The measurement results obtained from the opposite surfaces can provide a higher quality of the full-field strain evolution on the specimen. Therefore, we use the results obtained from the opposite surface measurements in the Results and Discussion sections of the main text. To further confirm the reliability of the results, we also provided the results of high-speed visual recording and the temperature fields on the same surface in the Supplementary Information (Supplementary Figs. 11 and 14).

Microstructure characterizations

The evolution of microstructural features before and after loading was observed using a scanning electron microscope (SEM) equipped with electron backscatter diffraction (EBSD). Sample preparation for EBSD analysis consisted of mechanical grinding followed by electropolishing using a Struers electropolisher with a solution of 5% perchloric acid, 80% butoxyethanol, and 15% methanol. The voltage was maintained at 40 V and the temperature at around −30 °C. The EBSD observations were made using a ZEISS Sigma 300 with an acceleration voltage of 20 kV. The selected scanning step was 0.03-0.2 μm. The EBSD data were analyzed using Aztec software. We also observed the microstructural features within the shear region after loading to the peak stress using a transmission electron microscope (TEM) to verify the dislocation configuration within the DRX grains. Due to the limited width of the localized shear zone, TEM samples were prepared using a dual-beam focused ion beam (FIB) system. They were then observed using a 300 KeV Tecnai F30 electron microscope.

Data availability

The authors declare that all relevant data supporting the findings of this study are available within the paper and its supplementary information files, or can be obtained from the corresponding author upon reasonable request.

Received: 7 June 2025; Accepted: 23 June 2025;
Published online: 05 July 2025

References

1. Bai Y. L., Dodd B., Adiabatic shear localization: occurrence, theories, and applications. 2nd ed. Oxford: Pergamon Press, 2012.
2. Meyers M. A., Dynamic Behavior of Materials, Wiley, New York, 1994.
3. Wright T. W., The Physics and Mathematics of Adiabatic Shear Bands, Cambridge University Press, Cambridge, New York, Port Melbourne, Madrid, Cape Town, 2002.
4. Meyers, M. A., Nesterenko, V. F., LaSalvia, J. C. & Xue, Q. Shear localization in dynamic deformation of materials: microstructural evolution and self-organization. *Mater. Sci. Eng. A* **317**, 204–225 (2001).
5. Meyers, M. A., Xu, Y. B., Xue, Q., Pérez-Prado, M. T. & McNelley, T. R. Microstructural evolution in adiabatic shear localization in stainless steel. *Acta Mater.* **51**, 1307–1325 (2003).
6. Antolovich, S. D. & Armstrong, R. W. Plastic strain localization in metals: origins and consequences. *Prog. Mater. Sci.* **59**, 1–160 (2014).
7. Viswanathan, K., Yadav, S. & Sagapuram, D. Shear bands in materials processing: understanding the mechanics of flow localization from Zener's time to the present. *Appl. Mech. Rev.* **72**, 060802 (2020).
8. Yan, N., Li, Z. Z., Xu, Y. B. & Meyers, M. A. Shear localization in metallic materials at high strain rates. *Prog. Mater. Sci.* **119**, 100755 (2021).
9. Zener, C. & Hollomon, J. H. Effect of strain rate upon plastic flow of steel. *J. Appl. Phys.* **15**, 22–32 (1944).

10. Marchand, A. & Duffy, J. An experimental study of the formation process of adiabatic shear bands in a structural steel. *J. Mech. Phys. Solids* **36**, 251–283 (1988).
11. Liao, S. & Duffy, J. Adiabatic shear bands in a Ti-6Al-4V titanium alloy. *J. Mech. Phys. Solids* **46**, 2201–2231 (1998).
12. Ranc, N., Taravella, L., Pina, V. & Herve, P. Temperature field measurement in titanium alloy during high strain rate loading—Adiabatic shear bands phenomenon. *Mech. Mater.* **40**, 255–270 (2008).
13. Wright, T. W. & Walter, J. W. On stress collapse in adiabatic shear bands. *J. Mech. Phys. Solids* **35**, 701–720 (1987).
14. Zhou, F., Wright, T. W. & Ramesh, K. T. The formation of multiple adiabatic shear bands. *J. Mech. Phys. Solids* **54**, 904–926 (2006).
15. Guo, Y. Z., Li, Y. L., Pan, Z., Zhou, F. H. & Wei, Q. A numerical study of microstructure effect on adiabatic shear instability: Application to nanostructured/ultrafine grained materials. *Mech. Mater.* **42**, 1020–1029 (2010).
16. Walley, S. M. Shear localization: a historical overview. *Metall. Mater. Trans. A* **38A**, 2629–2654 (2007).
17. Rittel, D., Wang, Z. G. & Merzer, M. Adiabatic shear failure and dynamic stored energy of cold work. *Phys. Rev. Lett.* **96**, 075502 (2006).
18. Guo, Y. Z. et al. Temperature rise associated with adiabatic shear band: causality clarified. *Phys. Rev. Lett.* **122**, 015503 (2019).
19. Zhu, S. X. et al. Formation of adiabatic shear band within Ti-6Al-4V: An in-situ study with high-speed photography and temperature measurement. *Inter. J. Mech. Sci.* **171**, 105401 (2020).
20. Guo, Y. Z. et al. Dynamic failure of titanium: Temperature rise and adiabatic shear band formation. *J. Mech. Phys. Solids* **135**, 103811 (2020).
21. Goviazin, G. G. & Rittel, D. Revisiting the hot adiabatic shear band paradigm. *Inter. J. Impact Eng.* **180**, 104702 (2023).
22. Rittel, D. & Wang, Z. G. Thermo-mechanical aspects of adiabatic shear failure of AM50 and Ti6Al4V alloys. *Mech. Mater.* **40**, 629–635 (2008).
23. Nie, Y. et al. In situ observation of adiabatic shear band formation in aluminum Alloys. *Exp. Mech.* **60**, 153–163 (2020).
24. Zeng, Q. L. et al. Two-dimensional evolution of temperature and deformation fields during dynamic shear banding: In-situ experiments and modeling. *Inter. J. Plast.***171**, 103782 (2023).
25. Kingstedt, O. T. & Lloyd, J. T. On the conversion of plastic work to heat in Mg alloy AZ31B for dislocation slip and twinning deformation. *Mech. Mater.* **134**, 176–184 (2019).
26. Nieto-Fuentes, J. C., Osovski, S., Venkert, A. & Rittel, D. Reassessment of the dynamic thermomechanical conversion in metals. *Phys. Rev. Lett.* **123**, 255502 (2019).
27. Xiong, Q. L., Li, Z. H., Shimada, T. & Kitamura, T. Atomistic investigation on the conversion of plastic work to heat in high-rate shear deformation. *Inter. J. Plast.***149**, 103158 (2022).
28. Padilla, H. A. II, Smith, C. D., Lambros, J., Beaudoin, A. J. & Robertson, I. M. Effects of deformation twinning on energy dissipation in high rate deformed zirconium. *Met. Mater. Trans. A* **38**, 2916–2927 (2007).
29. Rittel, D., Zhang, L. & Osovski, S. The dependence of the Taylor–Quinney coefficient on the dynamic loading mode. *J. Mech. Phys. Solids* **107**, 96–114 (2017).
30. Rittel, D., Landau, P. & Venkert, A. Dynamic recrystallization as a potential cause for adiabatic shear failure. *Phys. Rev. Lett.* **101**, 165501 (2008).
31. Medyanika, S. N., Liu, W. K. & Li, S. F. On criteria for dynamic adiabatic shear band propagation. *J. Mech. Phys. Solids* **55**, 1439–1461 (2007).
32. Longère, P. & Dragon, A. Enlarged finite strain modelling incorporating adiabatic shear banding and post-localization microvoiding as shear failure mechanisms. *Inter. J. Damage Mech.* **25**, 1142–1169 (2016).
33. Dorothy, H. L. & Longère, P. Modelling of high strain rate adiabatic shear banding induced failure: A comparison of two approaches. *Inter. J. Impact Eng.* **110**, 219–227 (2017).
34. Magagnosc, D. J., Lloyd, J. T., Meredith, C. S., Pilchak, A. L. & Schuster, B. E. Incipient dynamic recrystallization and adiabatic shear bands in Ti–7Al studied via in situ X-ray diffraction. *Inter. J. Plast.***141**, 102992 (2021).
35. Jiang, K. et al. Adiabatic shear localization induced by dynamic recrystallization in an FCC high entropy alloy. *Inter. J. Plast.***162**, 103550 (2023).
36. Yan, C. K. et al. Dynamic recrystallization of titanium: Effect of pre-activated twinning at cryogenic temperature. *Acta Mater.* **154**, 311–324 (2018).
37. Zhu, Z. C., Chen, Z. Y., Wang, R. K. & Liu, C. M. Forced shear deformation behaviors of annealed pure titanium under quasi-static and dynamic loading. *Mater. Sci. Eng. A* **839**, 142872 (2022).
38. Chouhan, D. K., Singh, A. K., Biswas, S. & Mondal, C. On the strain-hardening behavior and twin-induced grain refinement of CP-Ti under ambient temperature compression. *Metall. Mater. Trans. A* **50**, 2169–2188 (2019).
39. Wu, X. L. et al. Heterogeneous lamella structure unites ultrafine-grain strength with coarse-grain ductility. *P. Natl. Acad. Sci. USA* **112**, 14501–14505 (2015).
40. Su, W. L. et al. Heterostructure enables anomalous improvement of cryogenic mechanical properties in titanium. *Acta Mater.* **273**, 119982 (2024).
41. Dodd, B. & Atkins, A. G. Flow localization in shear deformation of void-containing and void-free solids. *Acta Metall.* **31**, 9–15 (1983).
42. McVeigh, C., Vernerey, F., Liu, W. K., Moran, B. & Olson, G. An interactive micro-void shear localization mechanism in high strength steels. *J. Mech. Phys. Solids* **55**, 225–244 (2007).
43. Kubair, D. V., Ramesh, K. T. & Swaminathan, P. K. Effect of shear-void-growth-softening on adiabatic shear-band-spacing in ductile materials. *Acta Mech.* **226**, 4189–4206 (2015).
44. Dorothy, H. L. & Longère, P. Unified modelling of adiabatic shear banding and subsequent micro-voiding driven dynamic failure of viscoplastic solids. *Inter. J. Impact Eng.* **132**, 103322 (2019).
45. Vishnu, A. R., Nieto-Fuentes, J. C. & Rodríguez-Martínez, J. A. Shear band formation in porous thin-walled tubes subjected to dynamic torsion. *Inter. J. Solids Struct.* **252**, 111837 (2022).
46. Vishnu, A. R., Marvi-Mashhadi, M., Nieto-Fuentes, J. C. & Rodríguez-Martínez, J. A. New insights into the role of porous microstructure on dynamic shear localization. *Inter. J. Plast.***148**, 103150 (2022).
47. Odeshi, A. G., Al-ameeri, S., Mirfakhraei, S., Yazdani, F. & Bassim, M. N. Deformation and failure mechanism in AISI 4340 steel under ballistic impact. *Theor. Appl. Fract. Mech.* **45**, 18–24 (2006).
48. Zeng, Q. L., Wang, T., Zhu, S. X., Chen, H. S. & Fang, D. N. A rate-dependent phase-field model for dynamic shear band formation in strength-like and toughness-like modes. *J. Mech. Phys. Solids* **164**, 104914 (2022).
49. Lu, L., Shen, Y. F., Chen, X. H., Qian, L. H. & Lu, K. Ultrahigh strength and high electrical conductivity in copper. *Science* **304**, 422–426 (2004).
50. De Cooman, B. C., Estrin, Y. & Kim, S. K. Twinning-induced plasticity (TWIP) steels. *Acta Mater.* **142**, 283–362 (2018).
51. Shawki, T. G. An energy criterion for the onset of shear localization in thermal viscoplastic materials, part i: Necessary and sufficient initiation conditions. *J. Appl. Mech.* **61**, 530–537 (1994).
52. Cherukuri, H. P. & Shawki, T. G. An energy-based localization theory: I. Basic framework. *Inter. J. Plast.***11**, 15–40 (1995).
53. Wright T. W. The Physics and Mathematics of Adiabatic Shear Bands, Cambridge University Press, 2002.
54. Tiamiyu, A. A. et al. Nanotwinning-assisted dynamic recrystallization at high strains and strain rates. *Nat. Mater.* **21**, 786–794 (2022).

55. Yang, D. K., Cizek, P., Hodgson, P. D. & Wen, C. E. Microstructure evolution and nanograin formation during shear localization in cold-rolled titanium. *Acta Mater.* **58**, 4536–4548 (2010).
56. Molodov, K. D., Al-Samman, T., Molodov, D. A. & Gottstein, G. Mechanisms of exceptional ductility of magnesium single crystal during deformation at room temperature: Multiple twinning and dynamic recrystallization. *Acta Mater.* **76**, 314–330 (2014).
57. Jia, D. et al. Deformation behavior and plastic instabilities of ultrafine-grained titanium. *Appl. Phys. Lett.* **79**, 611–613 (2001).
58. Sun, X. Y., Guo, Y. Z., Wei, Q., Li, Y. L. & Zhang, S. Y. A comparative study on the microstructure and mechanical behavior of titanium: Ultrafine grain vs. coarse grain. *Mater. Sci. Eng. A* **669**, 226–245 (2016).
59. Wang, M. S. et al. Superior strength-ductility synergy by microstructural heterogeneities in pure titanium. *Mater. Sci. Eng. A* **883**, 145513 (2023).

Acknowledgements

J. Li and T. Suo would like to thank the financial support from the National Natural Science Foundation of China (Grant Nos. 12025205, 12372366, 12102363, and 12141203). J. Li also thanked the financial support from Shanghai Central Guidance Fund for Local Science and Technology Development (Grant No. YDZX20233100004009). We also appreciate the technical support of microstructure characterizations from ZKKF Science & Technology, Inc. (Beijing).

Author contributions

J.G. Li and T. Suo designed the experiments. J.G. Zhong, J.M. Han, and L.K. Li conducted the mechanical tests and microstructure characterizations. J.G. Li, J.G. Zhong, H.S. Chen, Q. Wei and T. Suo analyzed and discussed the data and microscopic observations. J.G. Li wrote the manuscript draft; J.G. Li, Q. Wei, and T. Suo reviewed and revised the manuscript.

Competing interests

The authors declare no competing interests.

Additional information

Supplementary information The online version contains supplementary material available at https://doi.org/10.1038/s43246-025-00863-7.

Correspondence and requests for materials should be addressed to Jianguo Li, Qiuming Wei or Tao Suo.

Peer review information *Communications Materials* thanks the anonymous reviewers for their contribution to the peer review of this work. Primary Handling Editor: John Plummmer. A peer review file is available.